

Article

Analyzing Local Shear Rate Distribution in a Dual Coaxial Mixing Bioreactor Handling Herschel–Bulkley Biopolymer Solutions through Computational Fluid Dynamics

Forough Sharifi ¹, Ehsan Behzadfar ²  and Farhad Ein-Mozaffari ^{1,*} 

¹ Department of Chemical Engineering, Toronto Metropolitan University, 350 Victoria Street, Toronto, ON M5B 2K3, Canada; forough.sharifi@torontomu.ca

² Sustainable Polymers Research Lab, The Creative School, Toronto Metropolitan University, 350 Victoria Street, Toronto, ON M5B 2K3, Canada; behzadfar@torontomu.ca

* Correspondence: fmozaffa@torontomu.ca

Abstract: For the aeration of highly viscous non-Newtonian fluids, prior studies have demonstrated the improved efficacy of dual coaxial mixing bioreactors fitted with two central impellers and a close clearance anchor. Evaluating the effectiveness of these bioreactors involves considering various mixing characteristics, with a specific emphasis on shear rate distribution. The study of shear rate distribution is critical due to its significant impact on the mixing performance, gas dispersion, and homogeneity in aerated mixing systems comprising shear-thinning fluids. Although yield-pseudoplastic fluids are commonly employed in various industries, there is a research gap when it comes to evaluating shear rate distribution in aerated mixing bioreactors that utilize this fluid type. This study aims to investigate shear rate distribution in an aerated double coaxial bioreactor that handles a 1 wt% xanthan gum solution, known as a Herschel–Bulkley fluid. To achieve this goal, we employed an experimentally validated computational fluid dynamics (CFD) model to assess the effect of different mixing configurations, including down-pumping and co-rotating (Down-Co), up-pumping and co-rotating (Up-Co), down-pumping and counter-rotating (Down-Counter), and up-pumping and counter-rotating (Up-Counter) modes, on the shear rate distribution within the coaxial mixing bioreactor. Our findings revealed that the Up-Co system led to a more uniform local shear distribution and improved mixing performance.

Keywords: yield-pseudoplastic fluids; double coaxial mixing bioreactor; shear rate distribution; mixing configurations; computational fluid dynamics



Citation: Sharifi, F.; Behzadfar, E.; Ein-Mozaffari, F. Analyzing Local Shear Rate Distribution in a Dual Coaxial Mixing Bioreactor Handling Herschel–Bulkley Biopolymer Solutions through Computational Fluid Dynamics. *Processes* **2023**, *11*, 3387. <https://doi.org/10.3390/pr11123387>

Academic Editors: Giancarlo Cravotto and Pedro Fernandes

Received: 15 November 2023

Revised: 24 November 2023

Accepted: 1 December 2023

Published: 7 December 2023



Copyright: © 2023 by the authors. Licensee MDPI, Basel, Switzerland. This article is an open access article distributed under the terms and conditions of the Creative Commons Attribution (CC BY) license (<https://creativecommons.org/licenses/by/4.0/>).

1. Introduction

The majority of biological operations take place in the presence of aerobic microorganisms. The main goal of these processes is to provide sufficient oxygen in liquids for cell growth and the production of desired products, such as metabolites, enzymes, and proteins [1,2]. An inadequate level of oxygen in these processes can lead to impaired cell growth, altered metabolism, the accumulation of toxic compounds, and diminished product yields [3,4]. Therefore, finding an efficient bioreactor design that maintains a sufficient level of oxygen concentration in the fluid is essential, particularly for processes involving highly viscous non-Newtonian fluids. In fact, gas dispersion in bioreactors containing highly viscous non-Newtonian fluids presents challenges such as uneven distribution of gas bubbles, reduced gas–liquid contact area, lower mass transfer coefficient, increasing sensitivity to shear rate, scale-up complexities, fouling risks, and elevated power consumption [5,6].

Stirred bioreactors are superior compared to other aerated systems such as bubble columns and airlift bioreactors due to improved gas hold-up, a higher volumetric mass transfer coefficient, a more homogeneous shear rate distribution within the tank, and

a lower possibility of aggregate formation [7,8]. Despite their extensive range of applications in various industries, the effectiveness of aerated mixing bioreactors containing high-viscosity shear-thinning fluids faces challenges due to the uneven distribution of gas and shear forces [9]. Furthermore, due to the non-uniform distribution of shear rate, the stirring of yield-pseudoplastic fluids results in the formation of a thoroughly mixed zone near the impeller, commonly referred to as the “cavern”, with other areas remaining stationary [10,11]. This phenomenon is particularly notable within laminar and transitional flow regimes [12]. To address these issues, several studies demonstrated that intensifying operational conditions such as the impeller rotational speed and the aeration rate could positively influence mixing performance and offset the rise in broth viscosity [5,13]. In contrast, Jamshidzadeh et al. [14] reported instances of flooding and poor mixing patterns arising from higher aeration rates. Additionally, preventing the formation of high shear zones is crucial to avoid morphological damage to shear-sensitive microorganisms, especially in the case of plant or animal cells lacking protective cell walls [15].

In recent years, coaxial mixers integrating high-speed inner impellers alongside low-speed outer impellers have been introduced to confront the challenge of uneven gas and shear distribution encountered in traditional stirred bioreactors when dealing with highly viscous shear-thinning fluids. Coaxial mixers significantly improve mixing effectiveness by merging the benefits associated with both small-diameter and large-diameter impellers. The primary function of the low-speed outer impeller is to prevent the formation of stagnant zones by mobilizing the bulk fluid and the fluid adjacent to the tank walls [5,16,17]. In contrast, the high-speed inner impellers generate elevated shear rates in the center of the mixing tank, facilitating the breakup of bubbles. Over the past few years, research on the performance of aerated coaxial mixers handling highly viscous non-Newtonian fluids has primarily centered on analyzing gas hold-up, power consumption, and volumetric mass transfer coefficient [18–20]. Nevertheless, it is essential to acknowledge the growing significance of evaluating shear rate distribution within these systems. Shear-thinning fluids, characterized by decreasing viscosity as shear rates increase, introduce distinctive flow hydrodynamics when compared to Newtonian fluids, which significantly impact mass and momentum transfer as well as energy dissipation rates near the impeller [21]. Consequently, the focus has shifted towards studying shear rate distribution due to its substantial influence on enhancing gas dispersion efficiency and achieving system homogeneity. For instance, an even shear rate distribution promotes enhanced dispersion of gas bubbles, improved gas–liquid interactions, and uniform product quality. Sossa-Echeverria et al. [22] concluded that the comprehensive analysis of shear rate distribution enables the anticipation of flow patterns, optimization of power consumption, and identification of potential stagnation zones.

Both experimental and numerical methods have been employed to study factors affecting mixing effectiveness. Non-intrusive visualization methods, like particle image velocimetry (PIV), provide valuable insights into flow patterns by measuring tracer particle displacement to capture instantaneous velocity fields and related properties [22–24]. However, PIV, an experimental technique, necessitates transparent media for effective implementation [22]. This becomes a significant limitation when dealing with highly viscous non-Newtonian fluids with yield stress, as they are often opaque [25–27]. Consequently, conducting a comprehensive experimental investigation of fluid hydrodynamics within mixing systems containing such fluids becomes nearly impossible.

Computational fluid dynamics (CFD) is a powerful tool offering insights into the assessment of flow patterns and mixing characteristics that are often prohibitively expensive or simply unattainable through available experimental techniques [28–30]. This method provides comprehensive information regarding shear rates, flow patterns, velocity distributions, energy dissipation rate, power consumption, pumping capacities, and mixing time under various operating conditions [31,32]. Sossa-Echeverria et al. [22] employed computational fluid dynamics to explore the mixing performance of shear-thinning fluids with yield stress in a stirred tank equipped with various axial-flow impellers across laminar

to transitional flow regimes. Their findings demonstrated that the spatial distribution was determined using the trajectory of the impeller's discharge. However, while their CFD model effectively simulated the impact of operating conditions on mixing characteristics, it could not fully capture the flow symmetry observed in the experiments, which was attributed to limitations in the moving reference frame technique. Zang et al. [33] investigated the distribution of local shear rates in a stirred bioreactor containing pseudoplastic fluids near the impeller blade under a transitional flow regime using the CFD approach. They observed that the increase in consistency index and power-law index reduced the high-shear regions below the impeller blades. They showed that the influence of the impeller speed on the average local shear rate surpassed that of the rheological parameters. Furthermore, they showed that, given the complex dynamics of fluid flow in the vicinity of the impeller blade within stirred bioreactors with non-Newtonian fluids, the validated CFD model stands as a dependable approach that offers a comprehensive understanding of the flow phenomenon. This understanding, in turn, holds the potential to provide valuable insights for the optimization and design of stirred bioreactors.

Despite the widespread use of yield-pseudoplastic fluids across various industries, including food, chemical, biochemical, pharmaceutical, cosmetic production, and wastewater treatment plants, scarce information is available in the literature regarding the assessment of shear rate distribution in aerated mixing systems containing this type of media. Despite the recognized advantages of double coaxial stirred bioreactors compared to conventional systems, to the best of our knowledge, no prior study has investigated the distribution of the local shear rate in dual coaxial mixing bioreactors handling pseudoplastic fluids possessing yield stress. Therefore, this study addresses a significant research gap pertaining to the shear rate distribution in aerated coaxial mixing bioreactors that handle shear-thinning fluids with yield stress. The present work evaluates the influence of different mixing configurations, such as up-pumping and co-rotating (Up-Co), down-pumping and co-rotating (Down-Co), up-pumping and counter-rotating (Up-Counter), and down-pumping and counter-rotating (Down-Counter), on shear rate distribution within a double-aerated coaxial mixer containing 1 wt% xanthan gum solution, a pseudoplastic fluid with yield stress, using computational fluid dynamics (CFD). For this purpose, we employed a double coaxial mixing bioreactor with an aspect ratio greater than 1.0. This factor plays a critical role in ensuring the quality and consistency of the final product in the pharmaceutical, food processing, and cosmetics industries. The findings of this study contribute to understanding the behavior of aerated mixing of yield-pseudoplastic fluids and shed light on optimizing stirred bioreactors for improved shear distribution and gas dispersion.

2. Material and Methods

The experimental setup employed in this work consists of a flat-bottom cylindrical coaxial mixing tank with a diameter of 0.40 m, as depicted in Figure 1. The liquid level within the tank was maintained at a height of 0.50 m, resulting in a fluid volume of 0.063 m³ and an aspect ratio of 1.25. The coaxial mixer comprised two shafts: an upper shaft equipped with dual centrally positioned pitched-blade impellers and a lower shaft housing a close-clearance anchor impeller. These shafts were powered with two independent electric motors and regulated through frequency converters. Four distinct mixing configurations, namely Down-Co, Up-Co, Down-Counter, and Up-Counter, were examined in this study. A ring sparger featuring 20 holes was positioned at a clearance of 0.1 m from the tank base for introducing air into the system, and air dispersion within the system was regulated by measuring and controlling the airflow rate using a rotameter and a control valve, respectively.

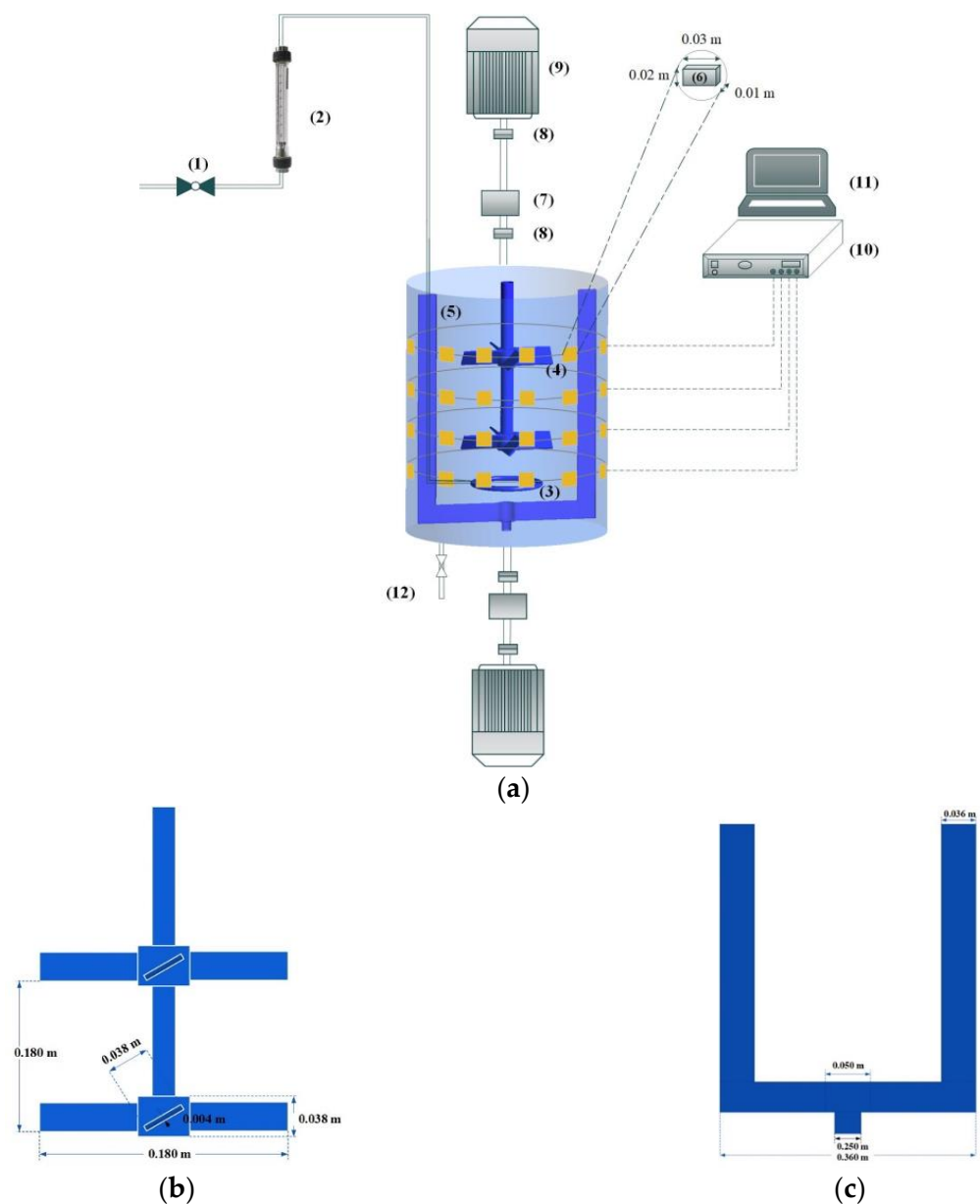


Figure 1. (a) Schematic diagram of experimental setup: (1) air control valve, (2) rotameter, (3) ring sparger, (4) pitched-blade turbine impellers, (5) anchor impeller, (6) ERT sensors, (7) torque meter, (8) couplings, (9) electric motor, (10) data acquisition system, (11) host computer, and (12) drain valve; (b) pitched-blade turbine impeller; and (c) anchor impeller.

2.1. Working Liquid

The aqueous solution of xanthan gum with a concentration of 1 wt% was employed as the working fluid. The rheological characteristics were assessed using a Kinexus Pro+ Rheometer (Malvern Instruments, Westborough, MA, USA). The rheological properties were measured using the shear rate table test at a constant temperature of 22 °C, which corresponds to the operating temperature of the experiments. Figure 2 displays the apparent viscosity and shear stress of the working fluid under varying shear rates. The working fluid exhibits shear-thinning behavior with yield stress. The rheological properties are closely aligned with the Herschel–Bulkley model for shear rates ranging from 0.1 to 100 L/s, and the corresponding model parameters are detailed in Table 1.

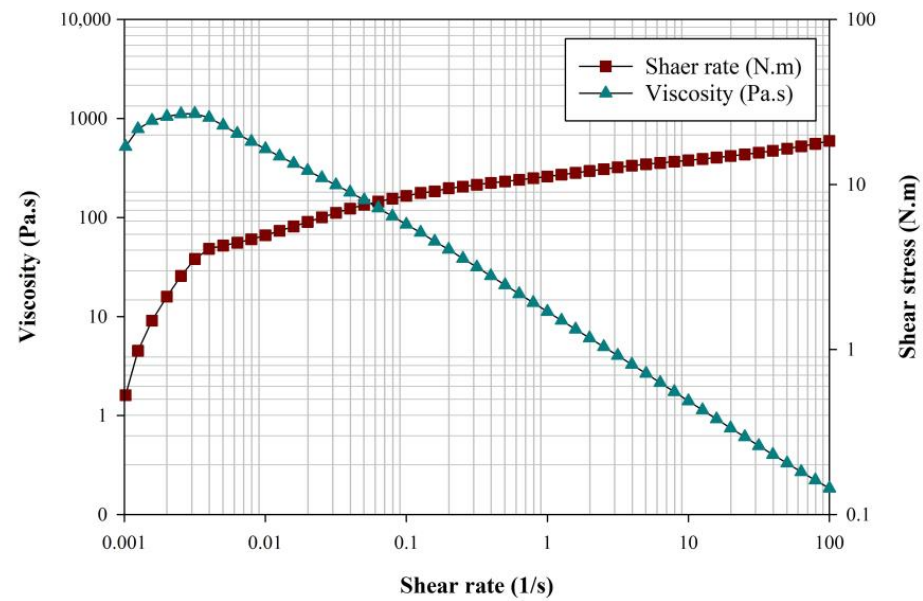


Figure 2. Rheological behavior of the xanthan gum solution with the concentration of 1 wt%.

Table 1. The rheological characteristic of the 1 wt% xanthan gum solution.

Density, ρ (kg/m ³)	Yield Stress, τ_y (Pa)	Consistency Index, k (Pa·s ^{n})	Power-Law Index (n)
983	3.22	10.16	0.13

2.2. Electrical Resistance Tomography (ERT)

In this work, both local and overall gas hold-ups were measured experimentally using the electrical resistance tomography (ERT) approach. For this purpose, the ERT system (Industrial Tomography Systems, model P2+) was used. As shown in Figure 1, the ERT system comprises four planes with 16 stainless steel electrodes on each plane, evenly distributed around the bioreactor tank. The ERT planes were labeled by number, and their heights from the bottom of the tank were: 0.38 m for plane 1, 0.27 m for plane 2, 0.22 m for plane 3, and 0.17 m for plane 4. A current of 5 mA with a frequency of 4800 Hz was applied to neighboring electrodes, and the voltages across consecutive pairs of these electrodes were recorded. This procedure was iterated to ascertain the local fluid conductivity. To mitigate the influence of the impellers, sparger, and shafts on fluid conductivity, 50 reference frames were recorded while the coaxial mixer rotated within a xanthan gum solution before introducing air. Subsequent to air introduction, an additional 50 frames were captured to establish a steady-state condition, and an extra 100 frames were recorded to quantify gas hold-up. It is important to mention that a minimum of 100 frames is essential for generating high-resolution tomography images and precisely assessing gas hold-up in the gas–liquid coaxial mixing bioreactors. Subsequently, the acquired data were sent to a data acquisition (DAQ) system for further processing. The linear back projection method was employed to reconstruct tomograms and analyze variations in the conductivity of the xanthan gum solution after air injection. Finally, the local fluid conductivity values were converted to local gas hold-ups using the Maxwell equation [34]:

$$\varepsilon_g = \frac{2\sigma_l + \sigma_g - 2\sigma_m \frac{\sigma_m \sigma_g}{\sigma_l}}{\sigma_m - \frac{\sigma_g}{\sigma_l} \sigma_m + 2(\sigma_l - \sigma_g)} \quad (1)$$

where ε_g , σ_l , σ_g , and σ_m represent the conductivity of the liquid, gas, gas–liquid mixture, and gas hold-up. Due to the negligible conductivity of the gas phase, the above equation can be simplified accordingly:

$$\varepsilon_g = \frac{2(\sigma_l - \sigma_m)}{2\sigma_l + \sigma_m} \quad (2)$$

2.3. Numerical Model

In this study, a fluid Eulerian–Eulerian approach was used to model the gas–liquid multiphase flow within the double coaxial mixing bioreactor. In this approach, both gas and liquid phases are considered interpenetrating continua; however, governing equations are independently solved for each phase [35]. The summation of the volume fractions of both phases is considered as one for all domains (Equation (3)). The continuity and momentum equations for each phase are presented in Equation (4) and Equation (5), respectively:

$$\varnothing_l + \varnothing_g = 1 \quad (3)$$

$$\frac{\partial(\rho_i \varnothing_i)}{\partial t} + \nabla \cdot (\rho_i \varnothing_i \vec{u}_i) = 0 \quad (4)$$

$$\frac{\partial(\varnothing_i \rho_i \vec{u}_i)}{\partial t} + \nabla \cdot (\varnothing_i \rho_i \vec{u}_i \vec{u}_i) = -\varnothing_i \nabla p + \nabla \cdot (\overline{\overline{\tau}}_{eff}) + \varnothing_i \rho_i g \pm F_i \quad (5)$$

In the above equations, ρ_i , \varnothing_i , u_i , and F_i are density, volume fraction, mean velocity, and the interface momentum exchange of phase i , respectively. Reynolds stress tensor, $\overline{\overline{\tau}}_{eff}$, as a function of time-averaged velocity is defined below [35]:

$$\overline{\overline{\tau}}_{eff} = \varnothing_i (\mu_i + \mu_{T,i}) (\nabla \vec{u}_i + \nabla \vec{u}_i^T) + (\lambda_i - \frac{2}{3} (\mu_i + \mu_{T,i})) \nabla \cdot \vec{u}_i \vec{I} \quad (6)$$

where λ_i is the bulk viscosity of the phase i and μ_i and $\mu_{T,i}$ are the laminar and turbulent viscosity of phase i , respectively.

In our prior research, we have demonstrated the accuracy of the modified Jamshidzadeh's correlation in reliably predicting the power number and Reynolds number [36]. Therefore, the apparent Reynolds number was estimated using Equation (7):

$$Re = \frac{\rho (f_{Pc} N_c + f_{Pa} N_a) (f_{Pc} D_c + f_{Pa} D_a)^2}{\frac{\tau_y}{K_s N_c} + k (K_s N_c)^{n-1}} \quad (7)$$

where

$$f_{Pc} = \frac{P_c}{P_t} \quad (8)$$

and

$$f_{Pa} = \frac{P_a}{P_t} \quad (9)$$

where f_{Pc} , f_{Pa} , and P_t are the central impeller power fraction, the anchor impeller power fraction, and the total gassed power consumption, respectively. N_a , N_c , D_c , and D_a are anchor speed, central impeller speed, anchor impeller diameter, and central impeller diameter, respectively. The Metzner–Otto constant (K_s) for the pitched blade turbine impeller was considered to be 12 [37]. Using Equation (7) and the rotational speeds of the impellers employed in this study, the range of Reynolds numbers for co-rotating and counter-rotating modes falls within $120 < Re < 2000$ and $150 < Re < 2200$, respectively. It is worth noting that the fully turbulent regime typically occurs when $Re \geq 10000$, while the laminar flow regime prevails when $Re \leq 10$ in stirred tanks. Consequently, the current flow regime in this study is transitional.

The interphase force, F_i (Equation (5)), is used to describe the interaction between the gas and liquid phases. In reality, fluid-induced forces such as drag, lift, and virtual mass all have an impact on the velocity of a bubble. However, several studies have demonstrated

that the only dominant force is the drag force, making it possible to ignore the impact of other interfacial forces [38–40].

Despite various drag models proposed in the literature to calculate the drag force in gas–liquid systems, the Schiller–Naumann drag model stands out for its accuracy in predicting mixing parameters. In addition, as reported in the literature, this model demonstrated the ability to effectively model the drag force for gas dispersion in non-Newtonian fluids under a laminar regime [41].

$$\vec{F}_{drag} = \frac{3}{4} \phi_g \phi_l \rho_l \frac{C_D}{d_b} |\vec{u}_g - \vec{u}_l| (\vec{u}_g - \vec{u}_l) \quad (10)$$

2.4. CFD Model

The 3D CFD modeling of the aerated double coaxial mixing bioreactor was developed using the commercial software ANSYS Fluent 2022 R1. Several studies have reported that assuming laminar flow in the transitional regime is justifiable when mixing shear-thinning fluids with yield stress [10,22]. Therefore, a laminar flow model was used in the simulations. The sliding mesh technique was employed to model the rotation of the impeller, enabling the transient simulation of the flow field. As shown in Figure 3, the fluid domain was discretized using non-uniform and unstructured tetrahedral elements. To assess the independence of the grid size on the simulation results, three distinct mesh configurations were employed in this study, consisting of 974,234, 1,843,861, and 3,642,931 mesh cells, respectively. The investigation of the impact of various mesh sizes on the xanthan gum velocity in the axial direction was carried out through simulations with three different mesh sizes: a coarse grid size (974,234), a medium grid size (1,843,861), and a fine grid size (3,642,931), with the corresponding results depicted in Figure 4. In this figure, the profiles of liquid velocity along the axial direction are depicted for three distinct grid sizes. Based on the data presented in this figure, it can be observed that the results obtained from the medium and fine grids exhibited negligible differences. Consequently, the grid with a size of 1,843,861 was chosen as the optimal mesh.

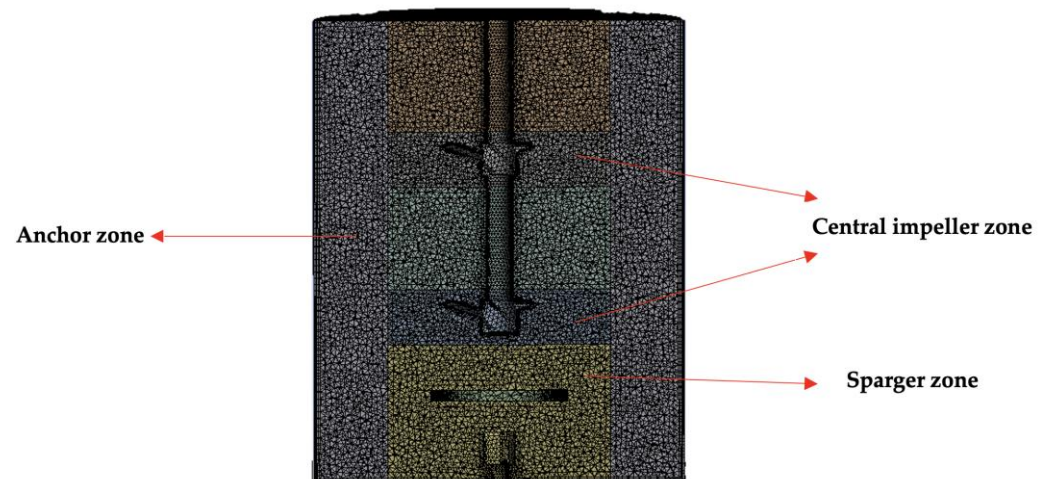


Figure 3. Computational grid structure of the double coaxial mixing bioreactor.

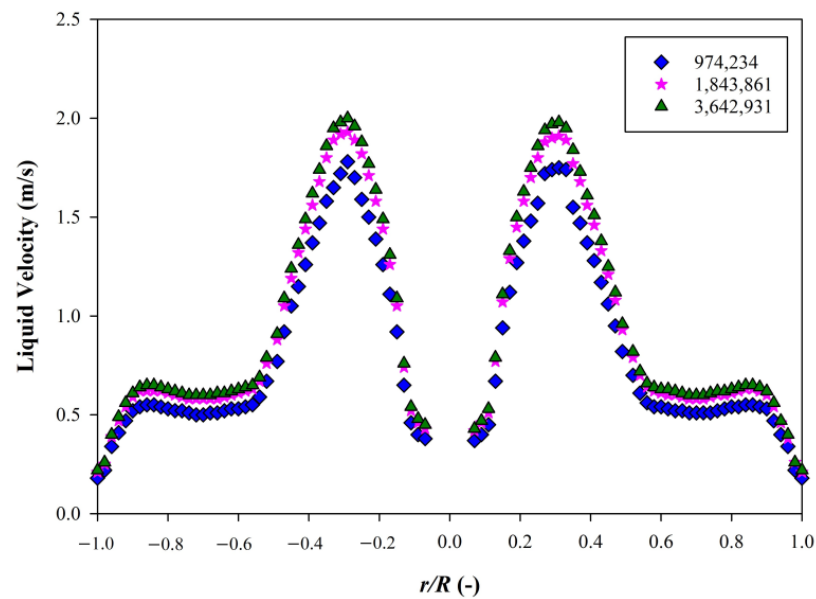


Figure 4. Grid independency test for three varying grid sizes.

The governing equations were solved using the finite volume method (FVM), and the pressure–velocity coupling was conducted using the SIMPLE technique. A second-order implicit scheme controlled time advancement, while a second-order upwind scheme discretized the momentum equation. To achieve convergence in each time step, 20 iterations were employed to ensure that the specified convergence tolerance of 10^{-7} was met for every normalized residual. Furthermore, the convergence of the model was verified by monitoring the dynamic profiles of gas hold-up in the four ERT planes. It was observed that nearly 72 revolutions of the central impeller were required for local gas hold-up profiles to attain a quasi-steady-state condition, indicating successful simulation convergence. To achieve convergence in each simulation, parallel computing with 12 CPUs was employed, with computational times ranging from 180 to 220 h.

The validation of the CFD model was performed by comparing the numerical results with experimental measurements of gassed power consumption and overall gas hold-up. The validation outcomes are displayed in Table 2. It is evident that there is a fairly good agreement between the experimental and CFD results, demonstrating the model’s predictive capability for other mixing characteristics.

Table 2. CFD model validation results for the Up-Co and Up-Counter modes at $N_c = 350$, $N_a = 10$ rpm, and $Q_g = 20$ L/min.

Mixing Configuration	Power Consumption (W)			Local Gas Hold-Up			
	EXP	CFD	Error%	EXP	CFD	Error%	
Up-Co	155.9	142.3	8.72	Plane 1	0.0520	0.0474	8.85
				Plane 2	0.0534	0.0496	7.12
				Plane 3	0.0509	0.0477	6.29
				Plane 4	0.0500	0.0472	5.60
Up-Counter	181.9	167.9	7.69	Plane 1	0.0407	0.0349	14.25
				Plane 2	0.0402	0.0370	7.96
				Plane 3	0.0386	0.0359	6.99
				Plane 4	0.0333	0.0310	6.91

3. Results and Discussion

The results obtained from the CFD model were used to compare the mixing characteristics of four mixing configurations, including Down-Co, Up-Co, Down-Counter, and

Up-Counter. For this purpose, local shear rate distribution, velocity fields, and dynamic viscosity were evaluated for different mixing configurations at varying rotational speeds of central impellers.

3.1. Comparing Different Mixing Configurations

Given the paramount importance of comprehending shear distribution in coaxial mixing bioreactors handling yield-pseudoplastic fluids, this study endeavors to investigate how various mixing configurations, namely Down-Co, Up-Co, Down-Counter, and Up-Counter, impact shear rate profiles within the system. In this regard, the shear rate contours were created using CFD post-processing within the range of 0.1 to 100 L/s, which aligns with the shear rate range selected for the rheological measurements. As depicted in Figure 5, a higher shear rate (indicated in red) was observed at the central impeller's blades, impeller discharge area, impeller swept zone, and tank wall. In general, a predominance of radial shear distribution was observed in the counter-rotation mode, whereas the co-rotating mode exhibited a more prominent axial shear distribution. For the Up-Co mode, the shear rate was distributed axially, which is attributed to the synergistic impact of the anchor and central impellers. In addition, in the vicinity of the tank wall, a higher shear rate was observed in the Up-Co configuration compared to other configurations, which reduced the likelihood of stationary zones.

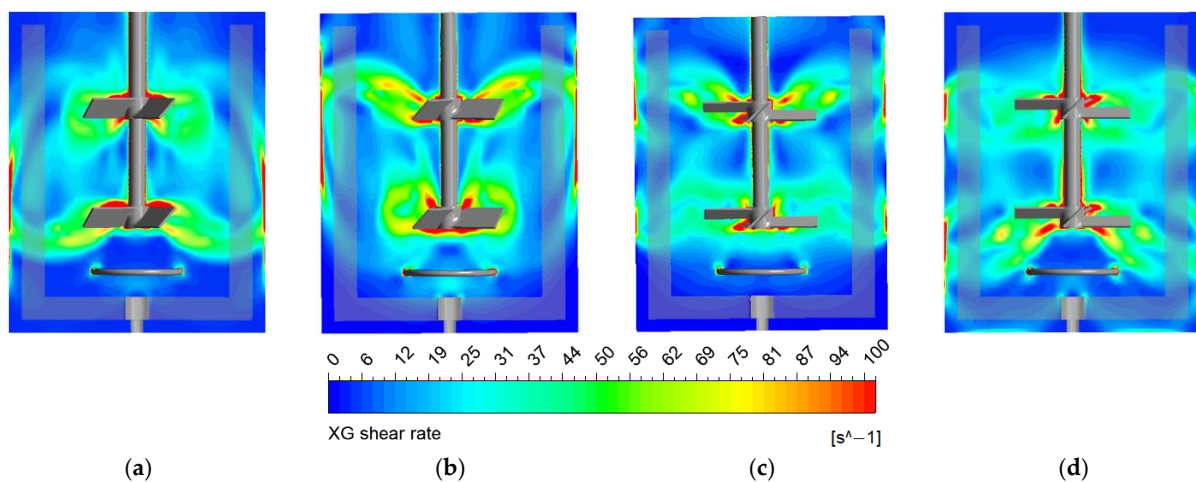


Figure 5. Local shear rate distribution for different mixing configurations: (a) Down-Co, (b) Up-Co, (c) Down-Counter, and (d) Up-Counter at $N_c = 350$ rpm, $N_a = 10$ rpm, and $Q_g = 20$ L/min.

The wider red areas were observed for the Up-Co mode around the impeller blades. Additionally, Figure 5 shows the presence of more uniformly distributed medium-shear zones in the axial direction for this configuration. When comparing the downward-pumping and upward-pumping in the co-rotating mode, it is evident that in the Down-Co mode, the area of high shear rate is limited to the vicinity of the central impellers, while a more homogeneous shear distribution was observed in the Up-Co mode.

The distribution of viscosity can be inferred from the shear rate contours due to the shear-thinning behavior displayed by the 1 wt% xanthan gum solution (Figure 6). As expected, lower apparent viscosities were observed in proximity to the impellers' discharge (indicated with a dark blue color) and along the tank wall, while an increase in viscosity was observed as the fluid moved away from the central impeller. In fact, high-viscosity regions were experienced below the sparger and near the liquid surface, while a reduction in viscosity occurred in the low-pressure zones created behind the blades, attributed to the acceleration of the rate of deformation caused by the central impellers. When comparing the shear distribution of all mixing configurations, the Up-Co mode showed a more uniform dynamic viscosity distribution, while the least uniformity was observed in the viscosity contours of the Down-Co and Down-Counter modes.

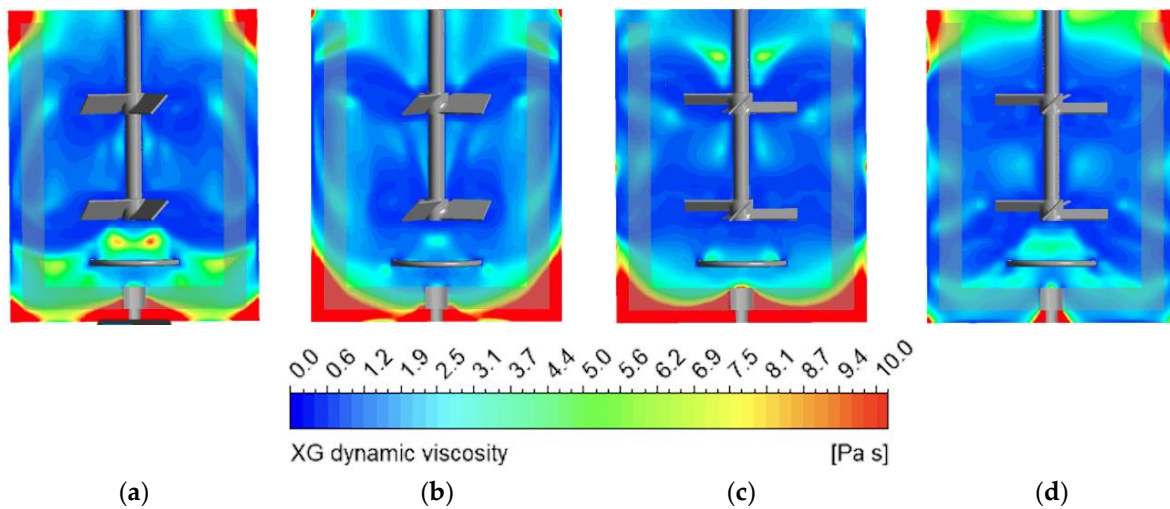


Figure 6. Local viscosity distribution for different mixing configurations: (a) Down-Co, (b) Up-Co, (c) Down-Counter, and (d) Up-Counter at $N_c = 350$ rpm, $N_a = 10$ rpm, and $Q_g = 20$ L/min.

To provide more insight, the local shear distribution contours were created on the radial planes at $y = 0.18$ m and $y = 0.36$ m (as depicted in Figure 7), corresponding to the centers of the top and bottom impellers, respectively. The red areas represent the high shear rates generated by the discharged jets from the central impeller through this plane. Similar to the axial shear rate contours, the radial shear rate contours for the Up-Co configuration illustrated a wider high-shear area surrounding the central impellers' blades and a more uniformly distributed shear rate, with large zones of medium shear rate values compared to the other mixing configurations. However, while the shear distribution near the central impeller in the Up-Counter mode closely resembles that of the Up-Co configuration, the presence of dark blue areas adjacent to the tank wall indicates insufficient shear dispersion in these regions. This deficit in shear distribution disrupts uniformity within the Up-Counter configuration.

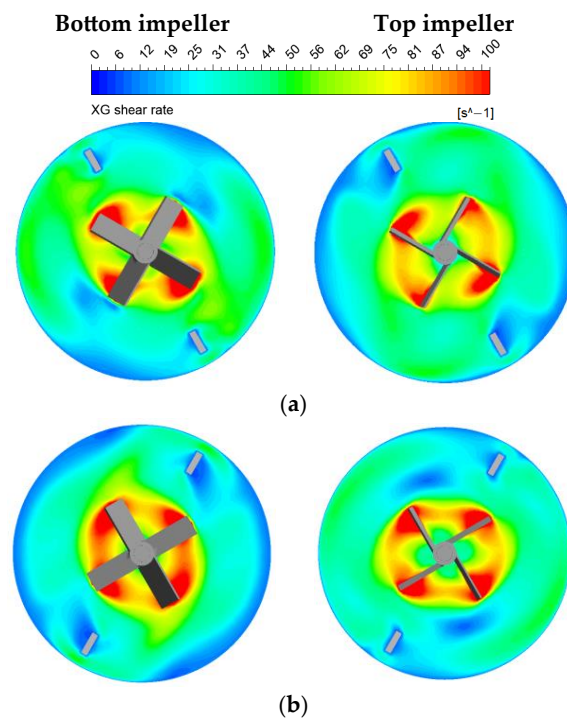


Figure 7. Cont.

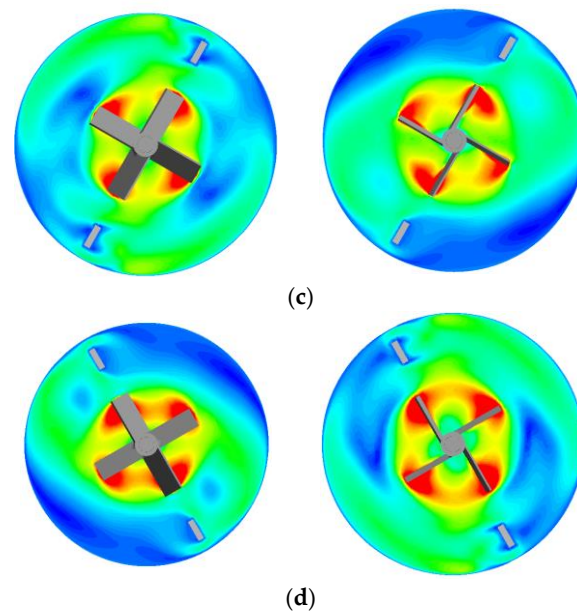


Figure 7. Radial distribution of shear rate in vicinity of the top and bottom central impellers: (a) Down-Co, (b) Up-Co, (c) Down-Counter, and (d) Up-Counter at $N_c = 350$ rpm, $N_a = 10$ rpm, and $Q_g = 20$ L/min.

The velocity fields were analyzed to conduct a more in-depth analysis of how mixing configurations affect shear rate distribution. Consequently, the velocity vectors were created for the 1 wt% xanthan gum solution over an axial plane for all configurations, including the Down-Co, Up-Co, Down-Counter, and Up-Counter, operating at $N_c = 350$ rpm, $N_a = 10$ rpm, and $Q_g = 20$ L/min, using CFD post-processing as shown in Figure 8. According to this figure, the high-speed red vectors represent the jets discharged from the central impellers, while the low-speed blue vectors indicate areas of slow motion. In a conventional double-mixing bioreactor without a close-clearance impeller, the radial jets discharged from the impeller move both upward and downward, forming upper and lower loops around each central impeller. Notably, Jamshidzadeh et al. [42] demonstrated that in a coaxial mixing system equipped with a close-clearance anchor and two central impellers, the synergistic effect of the anchor and central impellers led to the merging of the upper and lower loops, resulting in stable axial circulation loops in the middle of the tank, as shown in Figure 8a,b. When comparing the upward and downward pumping in the co-rotating mode, it became evident that while in the Down-Co configuration, the lower loops generated by the bottom impeller existed, the upper loops formed by the top impeller disappeared. This led to a significant reduction in the magnitude of the velocity vectors, resulting in decreased fluid motion near the anchor blades at the top part of the tank and a subsequent reduction in shear distribution in these areas. However, in the Up-Co mode, the upper loops generated by the top impeller ensured efficient mixing near the anchor blades at the top part of the tank.

In the counter-rotating mode, the circulation loops exhibited inconsistent shapes, resulting in small and disorderly circulation patterns in certain areas of the aerated tank. Additionally, a decrease in the magnitude of the velocity vector was observed at the top and bottom of the tank compared to the co-rotating mode, with a higher velocity observed around the central impellers (Figure 8c,d). Therefore, it can be concluded that the flow pattern generated by the counter-rotating mode led to compartmentalization within the coaxial mixing bioreactor, resulting in reduced axial flow from the top to the bottom of the system. For example, in the Up-Counter configuration, poor mixing was noted at the bottom of the tank, while in the Down-Counter configuration, insufficient mixing was noted in the upper section of the tank.

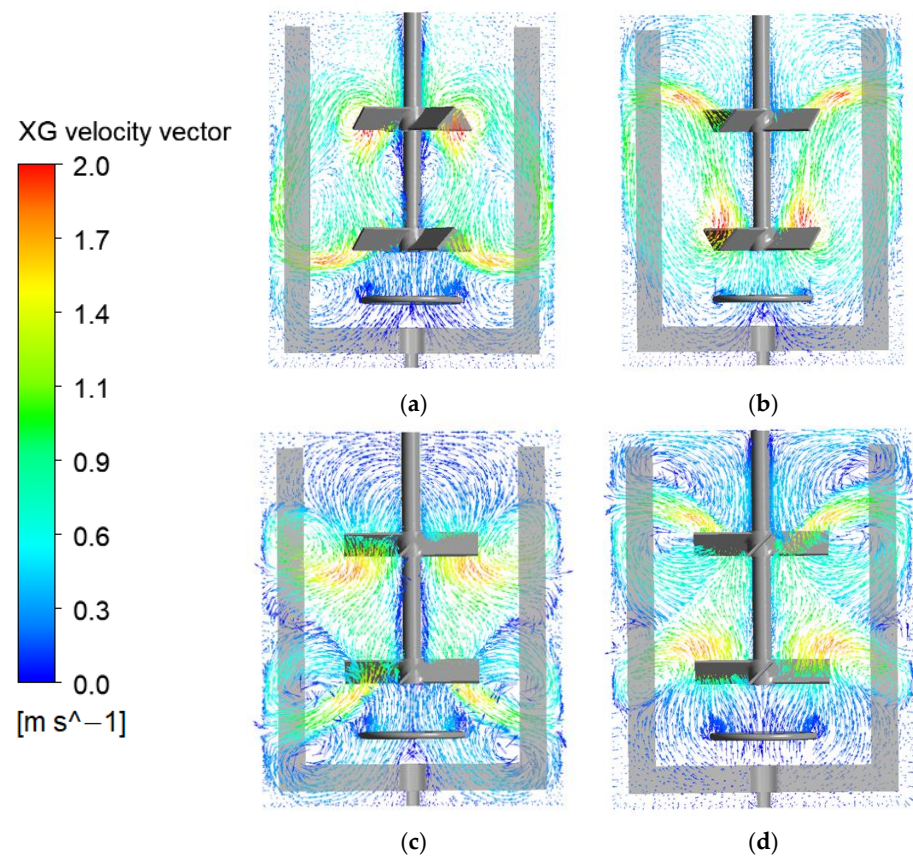


Figure 8. XG velocity vector plots for different mixing configurations: (a) Down-Co, (b) Up-Co, (c) Down-Counter, and (d) Up-Counter at $N_c = 350$ rpm, $N_a = 10$ rpm, and $Q_g = 20$ L/min.

Overall, when comparing all the velocity vectors of the xanthan gum solution obtained for all mixing configurations at $N_c = 350$ rpm and $N_a = 10$ rpm, it becomes evident that more efficient mixing occurs in the Up-Co mode. This accounts for the more uniform shear rate distribution in this configuration.

The quantitative analysis of xanthan gum velocity was conducted to provide a more comprehensive explanation of the velocity fields. In this context, profiles of normalized fluid velocity along a vertical line at $2r/D = 0.5$ were plotted for 1.0 wt% xanthan gum solution at $N_c = 350$ rpm and an aeration rate of 0.32 vvm for all configurations, including Down-Co, Up-Co, Down-Counter, and Up-Counter. It is important to note that the tip velocity of the central impellers ($\pi D_c N_c$) served as a reference for calculating the normalized fluid velocities. As depicted in Figure 9, the fluid velocity variation exhibited a bimodal distribution for all mixing configurations. The peaks on the plots correspond to the velocities of the jets discharged from each central impeller. Notably, the maximum velocity along the axial line is consistently lower than 60% of the central impeller tip speed (U_{tip}). This reduction is attributed to the high apparent viscosity of the xanthan gum solution. It can be inferred that the high apparent viscosity of the fluid led to resistance of the fluid to deformation, resulting in a lower transfer of shear rate generated by the impeller to the fluid and subsequently causing a decrease in the fluid velocity.

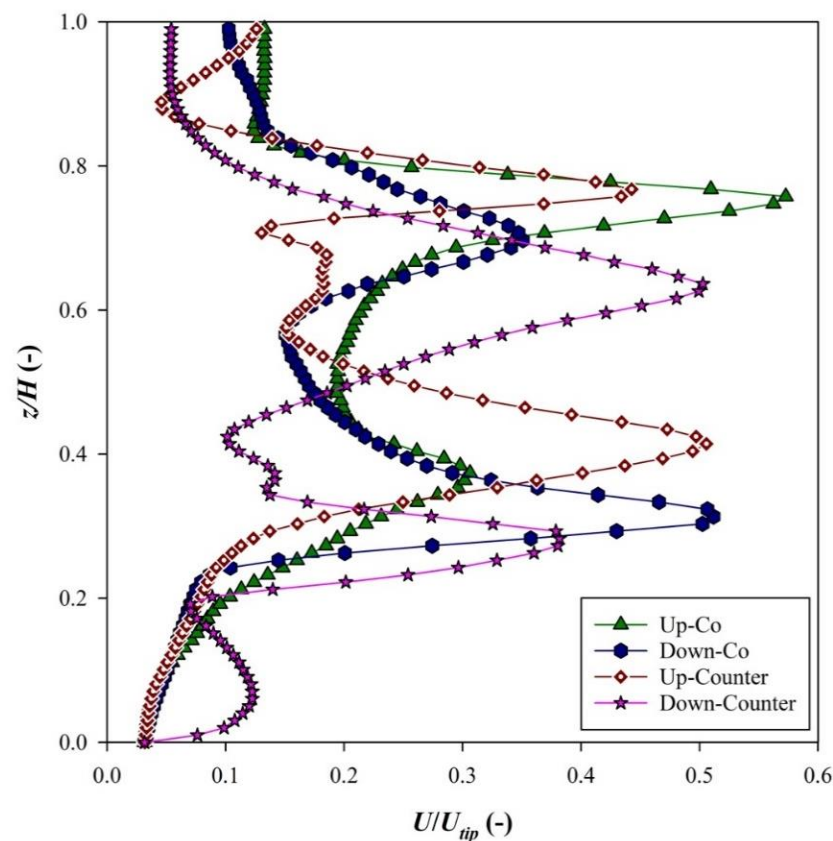


Figure 9. Axial profile of the normalized fluid velocity for all mixing configurations at $N_c = 350$ rpm, $N_a = 10$ rpm, and $Q_g = 20$ L/min.

According to Figure 9, in the co-rotating mode, the velocity peaks were observed in the vicinity of the central impeller. However, it was noted that in the Up-Counter mode, the lower peak shifted above the impeller blades, while the upper peak remained at the axial position of the upper impeller's blades. Conversely, in the Down-Counter mode, the axial position of the lower peak remained around the bottom impeller's blades, and the upper peak shifted below the blades of the top central impeller. This observation indicates that, in the counter-rotating mode, the axial positions of the upper and lower peaks were closer to each other, centered in the middle of the mixing tank. This phenomenon can be attributed to a reduced impeller pumping capacity in the counter-rotating mode. As a result, the lower fluid velocity and the closer peak positions in the counter-rotating mode diminished the efficient axial distribution of shear rate from top to bottom when compared to the co-rotating mode.

Figure 9 shows that the highest peak was located at the top central impeller in the Up-Co mode, while the highest peak at the bottom central impeller was observed in the Down-Co configuration. These observations are in agreement with the stable axial circulation loops seen in Figure 8a,b for the co-rotating mode, indicating that the higher fluid velocity in the co-rotating mode led to a greater impeller pumping capacity. Consequently, the fluid flow generated by the co-rotating mode was more directed in the axial direction compared to the counter-rotating mode. This finding corroborates the shear rate distribution seen in Figure 5.

3.2. The Effect of Central Impeller Speed

The substantial significance of the central impeller speed's influence on the shear rate distribution has been well-demonstrated in the literature [20]. Thus, this research aims to explore the effect of the central impeller speed on the shear distribution within a double coaxial mixer containing a 1 wt% xanthan gum solution. Therefore, both radial and

axial shear rate distributions were examined for Up-Co and Up-Counter configurations, as illustrated in Figure 10, at three different central impeller speeds: 250, 350, and 450 rpm. As shown in Figure 10 at $N_c = 250$ rpm, the shear rate distribution displayed non-uniformity in both the Up-Co and Up-Counter modes. The medium-shear rate regions (indicated in green) were observed around the central impellers, while dark blue regions at the lower and upper parts of the tank and near the tank wall indicated very low shear rates generated by the impellers in those areas.

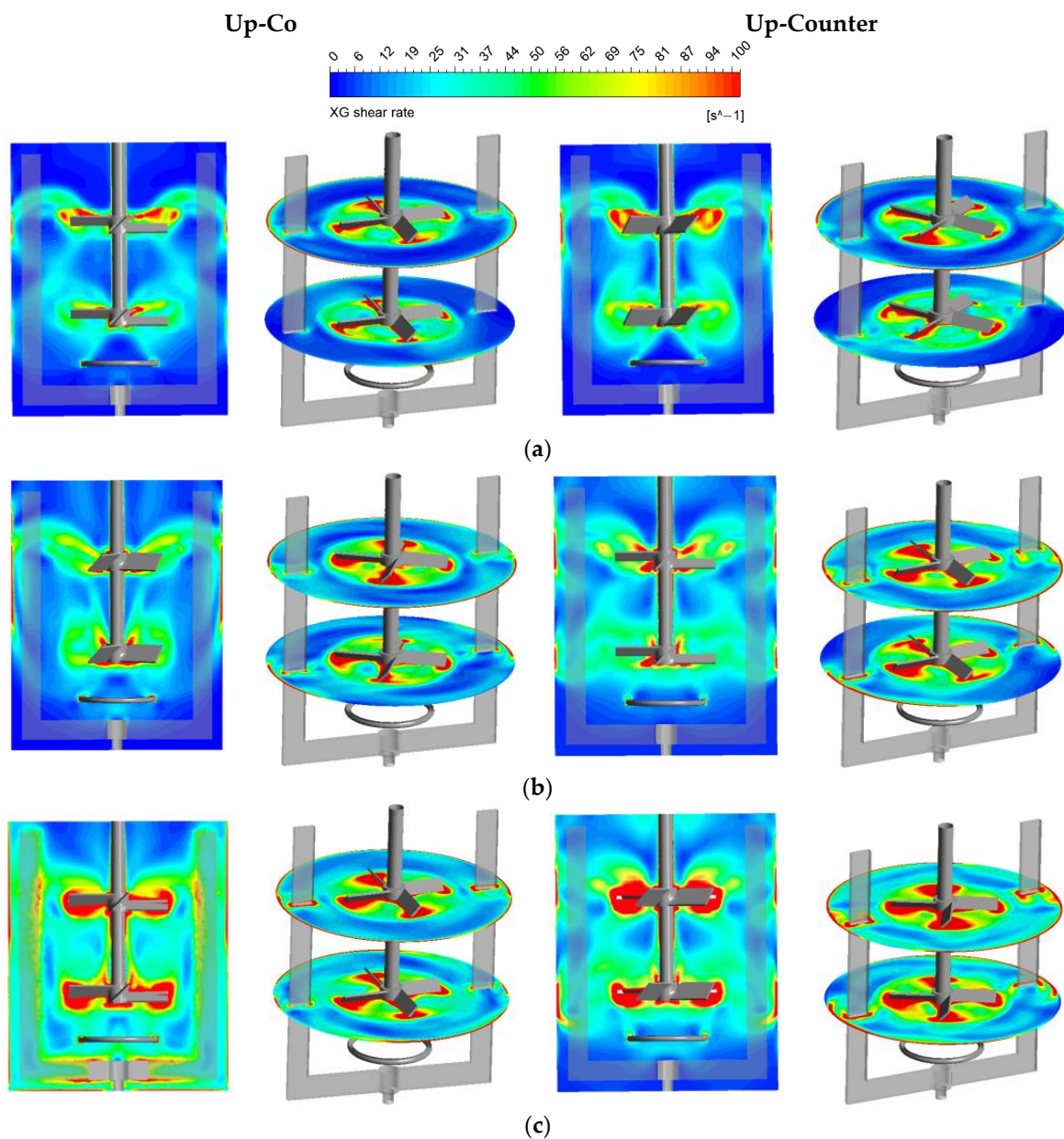


Figure 10. Shear rate contour at various central impeller speeds: (a) 250 rpm, (b) 350 rpm, and (c) 450 rpm at $N_d = 10$ rpm and $Q_g = 20$ L/min.

Elevating the central impeller speed to 450 rpm significantly enhanced both radial and axial shear distribution within the double coaxial bioreactor for both configurations. As shown in Figure 10c, in the Up-Co mode, raising the central impeller speed from 350 rpm to 450 rpm notably improved the uniformity of shear distribution within the system, particularly in the bottom half of the mixing tank, where shear rates had been very low at lower central impeller speeds. However, in the Up-Counter mode, while the shear rate

distribution considerably improved at $N_c = 450$ rpm compared to lower impeller speeds, the presence of the dark blue region in the lower part of the tank still indicates insufficient shear distribution in those areas.

As reported in the literature [14], designing efficient coaxial mixing bioreactors for pseudoplastic fluids with yield stress is crucial to eradicating or minimizing stagnant zones. CFD post-processing enables the identification of stagnant zones in mixing systems containing Herschel–Bulkley fluids by constraining the minimum shear rate in the shear rate contours to the critical shear rate value. To investigate the effect of increasing the central impeller speed on potential stagnant zones in a double coaxial bioreactor with pseudoplastic fluids possessing yield stress, shear rate contours were plotted for the Up-Co and Up-Counter modes at three central impeller speeds, as shown in Figure 11. To display stagnant zones in the shear rate contours, the minimum shear range was selected higher than the shear rate corresponding to the yield stress. Therefore, the uncolored regions in Figure 11 within the shear rate contours represent stagnant areas. According to this figure, the stagnant zones developed at the bottom of the tank for both the Up-Co and Up-Counter modes, with larger stagnant zones in the Up-Counter mode.

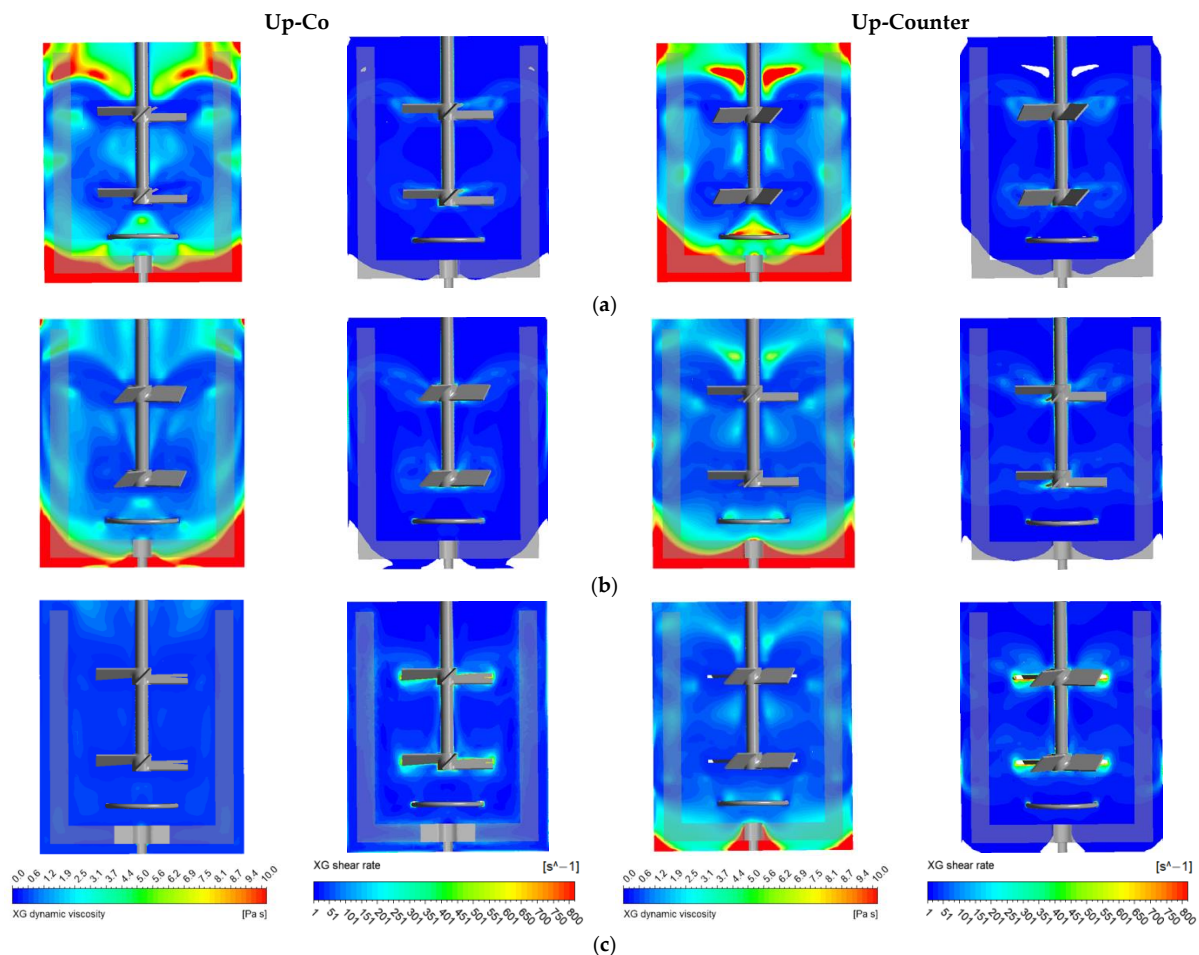


Figure 11. Impact of central impeller speed on the stagnant zones: (a) 250 rpm, (b) 350 rpm, and (c) 450 rpm.

Comparing shear rate contours with dynamic viscosity contours at $N_c = 250$ rpm revealed that the red regions in the dynamic viscosity contours corresponded to uncolored regions in the shear rate contours, confirming the presence of dead zones. Additionally, at $N_c = 250$ rpm, stagnant regions were observed above the top impeller in the Up-Counter mode, indicating inadequate mixing performance in this configuration. As the central impeller speed increased, the size of the undesired dead zone decreased, showing the

positive impact of higher central impeller speeds on mixing performance. Interestingly, elevating the central impeller speed to 450 rpm in the Up-Co mode prevented the formation of undesired dead zones, enhancing fluid mixing effectiveness. However, small stagnant zones were still observed at the bottom corner and around the anchor impeller shaft in the Up-Counter configuration.

In order to further elaborate on the positive contribution of increasing the central impeller speed to eliminating dead zones, the radial profile of the normalized liquid axial velocity is depicted in Figure 12 at $z/H = 0.54$ for both the Up-Co and Up-Counter modes. It should be noted that in this profile, the location of the central impeller blade tip is at $2r/D = \pm 0.45$. It was observed that, for both configurations at $N_c = 250$ rpm, the distribution of liquid axial velocity was mostly radial in the region from the impeller tip to the tank wall. This indicates that the axial flow was not effectively generated by the central impellers at low rotational speeds. However, in the Up-Co mode, with a further increase in the central impeller speed, a negative peak was observed between the shaft and the central impeller tip, while a positive peak was observed at the anchor blades. Similarly, this pattern was observed for the Up-Counter configuration.

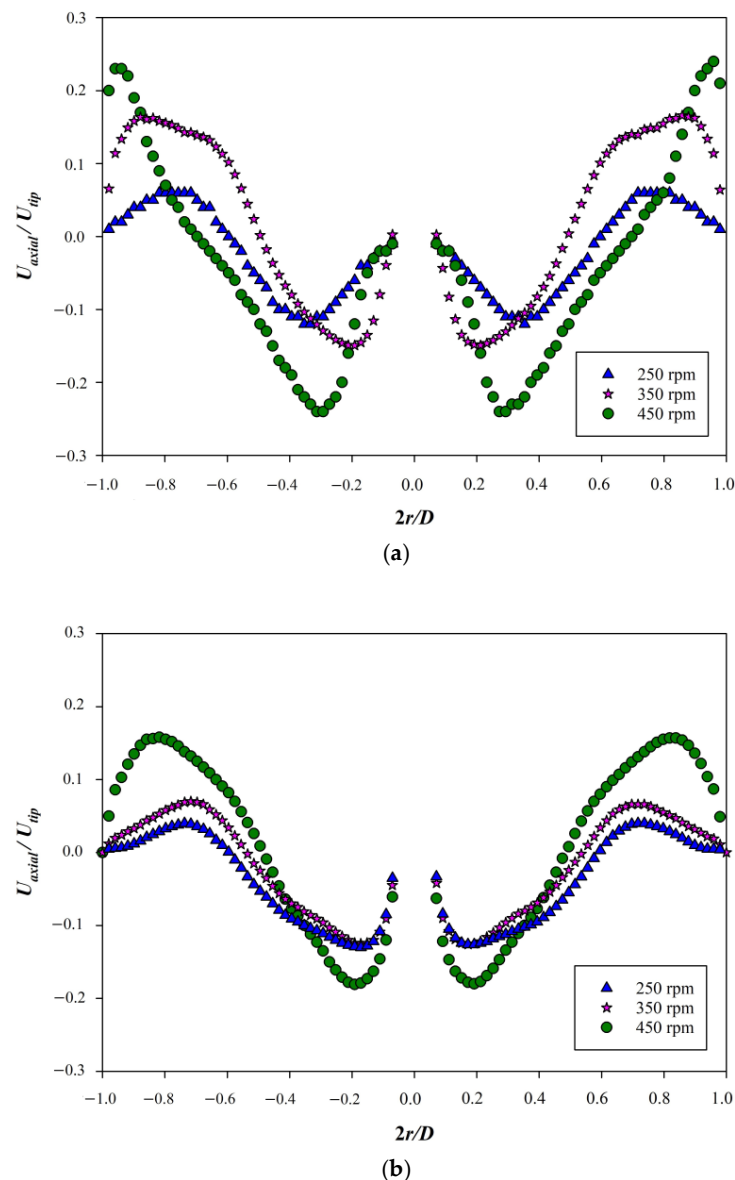


Figure 12. Radial profile of dimensionless liquid axial velocity for: (a) Up-Co, (b) Up-Counter modes at $z/H = 0.54$ at $N_a = 10$ rpm and $Q_3 = 20$ L/min.

As reported in the literature, the transition in the axial velocity from positive to negative affirms the existence of circulation loops [5]. Additionally, the values of both negative and positive peaks of the normalized axial velocity increased with a further increase in the central impeller speed, demonstrating the development of stronger circulation loops, which is in line with the findings in Figure 8. It is noteworthy that higher values of the axial liquid velocity were obtained in the Up-Co mode compared to the Up-Counter mode, once again indicating enhanced flow hydrodynamics in the Up-Co mode.

4. Conclusions

In conclusion, this study thoroughly explored the mixing characteristics of four mixing configurations, namely Down-Co, Up-Co, Down-Counter, and Up-Counter, within a double coaxial mixing bioreactor handling a 1 wt% xanthan gum solution with yield stress. The investigation encompassed an extensive analysis of local shear rate distribution, velocity fields, and dynamic viscosity under varying central impeller speeds. The findings revealed that the choice of mixing configuration significantly impacts shear rate profiles within the system. The mixing configurations in the co-rotating mode (Up-Co and Down-Co) exhibited distinct shear distributions, with the Up-Co mode offering a more prominent axial shear distribution and superior shear uniformity. In contrast, the coaxial mixing systems in the counter-rotating mode (Down-Counter and Up-Counter) exhibited radial shear predominance and less uniform shear rate distribution, resulting in compartmentalization within the reactor. Furthermore, this study demonstrated the crucial role of central impeller speed in shear rate distribution. Higher impeller speeds led to improved shear uniformity, particularly in the bottom half of the tank, and reduced the presence of stagnant zones. In particular, the Up-Co mode at higher impeller speeds showcased enhanced mixing effectiveness and the prevention of undesired dead zones.

Author Contributions: Conceptualization, F.S., E.B. and F.E.-M.; Methodology, F.S.; Software, F.S.; Validation, F.S.; Formal analysis, F.S.; Investigation, F.S.; Resources, E.B. and F.E.-M.; Writing—original draft, F.S.; Writing—review & editing, E.B. and F.E.-M.; Supervision, E.B. and F.E.-M.; Project administration, E.B. and F.E.-M.; Funding acquisition, E.B. and F.E.-M. All authors have read and agreed to the published version of the manuscript.

Funding: We express profound gratitude for the financial assistance offered by Natural Sciences and Engineering Research Council of Canada (NSERC) under grant number RGPIN-2019-04644.

Data Availability Statement: The data will be available upon request.

Acknowledgments: We appreciate ANSYS for granting us a license and acknowledge Niagara for generously providing supercomputer resources for our computational fluid dynamics simulations.

Conflicts of Interest: The authors declare no conflict of interest.

Nomenclature

D	Tank diameter, m
D_c	Diameter of the central impeller, m
f_{pa}	The ratio of the anchor power to the total power, dimensionless
f_{pc}	The ratio of the central impeller power to the total power, dimensionless
F_i	Interface momentum exchange, N
H	Height of the tank, m
k	Consistency index, Pa.s ⁿ
K_s	Metzner and Otto constant
n	Power index, dimensionless
N_c	Central impeller rotational speed, rpm
N_a	Anchor impeller rotational speed, rpm
Q_g	Volumetric flow rate of the gas, L/min
Re	Reynolds number, dimensionless
r	Radius, m

R	Tank radius, m
U_{axial}	Liquid axial velocity, m/s
U_{tip}	Impeller tip velocity, m/s
U	Liquid velocity in stationary frame, m/s
z	Height, m

Greek letters

$\dot{\gamma}$	Shear rate, L/s
ε_g	Gas hold-up, dimensionless
λ	Bulk viscosity, Pa.s
μ	Laminar viscosity, Pa.s
μ_T	Turbulent viscosity, Pa.s
ρ	Density of liquid, kg/m ³
σ_g	Gas conductivity, S/cm
σ_l	Liquid conductivity, S/cm
σ_{mc}	Mixture conductivity, S/cm
τ	Shear stress, Pa
$\overline{\tau}_{eff}$	Reynolds stress tensor, Pa
τ_y	Yield stress, Pa
ϕ	Volume fraction, dimensionless

References

- Paulová, L.; Patáková, P.; Brányik, T. Advanced fermentation processes. In *Engineering Aspects of Food Biotechnology*; CRC Press: Boca Raton, FL, USA, 2013; pp. 89–110. [\[CrossRef\]](#)
- Wang, S.J.; Zhong, J.J. Bioreactor engineering. In *Bioprocessing for Value-Added Products from Renewable Resources*; Elsevier: Amsterdam, The Netherlands, 2007; pp. 131–161.
- Moucha, T.; Linek, V.; Prokopová, E. Gas hold-up, mixing time and gas–liquid volumetric mass transfer coefficient of various multiple-impeller configurations: Rushton turbine, pitched blade and techmix impeller and their combinations. *Chem. Eng. Sci.* **2003**, *58*, 1839–1846. [\[CrossRef\]](#)
- Dhanasekharan, K.M.; Sanyal, J.; Jain, A.; Haidari, A. A generalized approach to model oxygen transfer in bioreactors using population balances and computational fluid dynamics. *Chem. Eng. Sci.* **2005**, *60*, 213–218. [\[CrossRef\]](#)
- Sharifi, F.; Behzadfar, E.; Ein-Mozaffari, F. Intensified gas-liquid mixing in bioreactors equipped with a dual coaxial mixer containing biopolymer solutions. *Chem. Eng. Res. Des.* **2023**, *191*, 109–126. [\[CrossRef\]](#)
- Terasaka, K.; Shibata, H. Oxygen transfer in viscous non-Newtonian liquids having yield stress in bubble columns. *Chem. Eng. Sci.* **2003**, *58*, 5331–5337. [\[CrossRef\]](#)
- De Jesus, S.S.; Neto, J.M.; Maciel Filho, R. Hydrodynamics and mass transfer in bubble column, conventional airlift, stirred airlift and stirred tank bioreactors, using viscous fluid: A comparative study. *Biochem. Eng. J.* **2017**, *118*, 70–81. [\[CrossRef\]](#)
- Núñez EG, F.; Leme, J.; de Almeida Parizotto, L.; Chagas, W.A.; de Rezende, A.G.; da Costa BL, V.; Monteiro DC, V.; Boldorini VL, L.; Jorge SA, C.; Astray, R.M.; et al. Influence of aeration–homogenization system in stirred tank bioreactors, dissolved oxygen concentration and pH control mode on BHK-21 cell growth and metabolism. *Cytotechnology* **2014**, *66*, 605–617. [\[CrossRef\]](#)
- Tang, W.; Pan, A.; Lu, H.; Xia, J.; Zhuang, Y.; Zhang, S.; Chu, J.; Noorman, H. Improvement of glucoamylase production using axial impellers with low power consumption and homogeneous mass transfer. *Biochem. Eng. J.* **2015**, *99*, 167–176. [\[CrossRef\]](#)
- Arratia, P.E.; Kukura, J.; Lacombe, J.; Muzzio, F.J. Mixing of shear-thinning fluids with yield stress in stirred tanks. *AIChE J.* **2006**, *52*, 2310–2322. [\[CrossRef\]](#)
- Jaworski, Z.; Pacek, A.W.; Nienow, A.W. On flow close to cavern boundaries in yield stress fluids. *Chem. Eng. Sci.* **1994**, *49*, 3321–3324. [\[CrossRef\]](#)
- Adams, L.W.; Barigou, M. CFD analysis of caverns and pseudo-caverns developed during mixing of non-Newtonian fluids. *Chem. Eng. Res. Des.* **2007**, *85*, 598–604. [\[CrossRef\]](#)
- Wang, S.; Li, H.; Tao, C.; Liu, R.; Wang, Y.; Liu, Z. Study on cavern evolution and performance of three mixers in agitation of yield-pseudoplastic fluids. *Chin. J. Chem. Eng.* **2023**, *55*, 111–122. [\[CrossRef\]](#)
- Jamshidzadeh, M.; Ein-Mozaffari, F.; Lohi, A. Local and overall gas holdup in an aerated coaxial mixing system containing a non-Newtonian fluid. *AIChE J.* **2020**, *66*, e17016. [\[CrossRef\]](#)
- García-Ochoa, F.; Gómez, E. Bioreactor scale-up and oxygen transfer rate in microbial processes: An overview. *Biotechnol. Adv.* **2009**, *27*, 153–176. [\[CrossRef\]](#)
- Foucault, S.; Ascanio, G.; Tanguy, P.A. Power characteristics in coaxial mixing: Newtonian and non-Newtonian fluids. *Ind. Eng. Chem. Res.* **2005**, *44*, 5036–5043. [\[CrossRef\]](#)
- Thibault, F.; Tanguy, P.A. Power-draw analysis of a coaxial mixer with Newtonian and non-Newtonian fluids in the laminar regime. *Chem. Eng. Sci.* **2002**, *57*, 3861–3872. [\[CrossRef\]](#)

18. Rahimzadeh, A.; Ein-Mozaffari, F.; Lohi, A. Scale-up study of aerated coaxial mixing reactors containing non-newtonian power-law fluids: Analysis of gas holdup, cavity size, and power consumption. *J. Ind. Eng. Chem.* **2022**, *113*, 293–315. [[CrossRef](#)]
19. Rahimzadeh, A.; Ein-Mozaffari, F.; Lohi, A. Investigation of power consumption, torque fluctuation, and local gas hold-up in coaxial mixers containing a shear-thinning fluid: Experimental and numerical approaches. *Chem. Eng. Process.-Process Intensif.* **2022**, *177*, 108983. [[CrossRef](#)]
20. Amirafabi, M.; Khiadani, M.; Mohammed, H.A. Performance of a dual helical ribbon impeller in a two-phase (gas-liquid) stirred tank reactor. *Chem. Eng. Process.-Process Intensif.* **2020**, *148*, 107811. [[CrossRef](#)]
21. Ameer, H.; Bouzit, M. Mixing in shear thinning fluids. *Braz. J. Chem. Eng.* **2012**, *29*, 349–358. [[CrossRef](#)]
22. Sossa-Echeverria, J.; Taghipour, F. Computational simulation of mixing flow of shear thinning non-Newtonian fluids with various impellers in a stirred tank. *Chem. Eng. Process. Process Intensif.* **2015**, *93*, 66–78. [[CrossRef](#)]
23. Ciou, Z.Y.; Wu, C.Y. Investigation of the flow patterns and mixing efficiency in a stirred tank through particle image velocimetry. *J. Taiwan Inst. Chem. Eng.* **2023**, *149*, 104988. [[CrossRef](#)]
24. Laakkonen, M.; Honkanen, M.; Saarenrinne, P.; Aittamaa, J. Local bubble size distributions, gas-liquid interfacial areas and gas holdups in a stirred vessel with particle image velocimetry. *Chem. Eng. J.* **2005**, *109*, 37–47. [[CrossRef](#)]
25. Fontaine, A.; Guntzburger, Y.; Bertrand, F.; Fradette, L.; Heuzey, M.C. Experimental investigation of the flow dynamics of rheologically complex fluids in a Maxblend impeller system using PIV. *Chem. Eng. Res. Des.* **2013**, *91*, 7–17. [[CrossRef](#)]
26. Alberini, F.; Liu, L.; Stitt, E.H.; Simmons MJ, H. Comparison between 3-D-PTV and 2-D-PIV for determination of hydrodynamics of complex fluids in a stirred vessel. *Chem. Eng. Sci.* **2017**, *171*, 189–203. [[CrossRef](#)]
27. Ayala, J.S.; de Moura, H.L.; de Lima Amaral, R.; Júnior FD, A.O.; Nunhez, J.R.; de Castilho, G.J. Two-dimensional shear rate field and flow structures of a pseudoplastic fluid in a stirred tank using particle image velocimetry. *Chem. Eng. Sci.* **2022**, *248*, 117198. [[CrossRef](#)]
28. Wang, H.; Jia, X.; Wang, X.; Zhou, Z.; Wen, J.; Zhang, J. CFD modeling of hydrodynamic characteristics of a gas-liquid two-phase stirred tank. *Appl. Math. Model.* **2014**, *38*, 63–92. [[CrossRef](#)]
29. Jia, Z.; Xu, L.; Duan, X.; Mao, Z.S.; Zhang, Q.; Yang, C. CFD simulation of flow and mixing characteristics in a stirred tank agitated by improved disc turbines. *Chin. J. Chem. Eng.* **2022**, *50*, 95–107. [[CrossRef](#)]
30. Wang, H.; Duan, X.; Feng, X.; Mao, Z.S.; Yang, C. Effect of impeller type and scale-up on spatial distribution of shear rate in a stirred tank. *Chin. J. Chem. Eng.* **2022**, *42*, 351–363. [[CrossRef](#)]
31. Ihejirika, I.; Ein-Mozaffari, F. Using CFD and ultrasonic velocimetry to study the mixing of pseudoplastic fluids with a helical ribbon impeller. *Chem. Eng. Technol. Ind. Chem.-Plant Equip.-Process Eng.-Biotechnol.* **2007**, *30*, 606–614. [[CrossRef](#)]
32. Kumaresan, T.; Joshi, J.B. Effect of impeller design on the flow pattern and mixing in stirred tanks. *Chem. Eng. J.* **2006**, *115*, 173–193. [[CrossRef](#)]
33. Zhang, Y.; Wang, L.; Huo, H.; Li, Z.; Gao, Z. Computational and experimental investigation of flow fields in a Rushton turbine stirred tank with shear-thinning fluid. *Asia-Pac. J. Chem. Eng.* **2022**, *17*, e2735. [[CrossRef](#)]
34. Maxwell, J.C. *A Treatise on Electricity and Magnetism: Pt. III. Magnetism. pt. IV. Electromagnetism*; Clarendon Press: Oxford, UK, 1881; Volume 2.
35. Ansys Fluent. *Ansys Fluent Theory Guide*; Ansys Inc.: Canonsburg, PA, USA, 2011; Volume 15317, pp. 724–746.
36. Sharifi, F.; Behzadfar, E.; Ein-Mozaffari, F. Investigating the Power Consumption for the Intensification of Gas Dispersion in a Dual Coaxial Mixer Containing Yield-Pseudoplastic Fluids. *Chem. Eng. Process.-Process Intensif.* **2023**, *191*, 109461. [[CrossRef](#)]
37. Kelly, W.; Gigas, B. Using CFD to predict the behavior of power law fluids near axial-flow impellers operating in the transitional flow regime. *Chem. Eng. Sci.* **2003**, *58*, 2141–2152. [[CrossRef](#)]
38. Scargiali, F.; D’Orazio, A.; Grisafi, F.; Brucato, A. Modelling and simulation of gas-liquid hydrodynamics in mechanically stirred tanks. *Chem. Eng. Res. Des.* **2007**, *85*, 637–646. [[CrossRef](#)]
39. Jahoda, M.; Tomášková, L.; Moštěk, M. CFD prediction of liquid homogenisation in a gas-liquid stirred tank. *Chem. Eng. Res. Des.* **2009**, *87*, 460–467. [[CrossRef](#)]
40. Khopkar, A.R.; Kasat, G.R.; Pandit, A.B.; Ranade, V.V. CFD simulation of mixing in tall gas-liquid stirred vessel: Role of local flow patterns. *Chem. Eng. Sci.* **2006**, *61*, 2921–2929. [[CrossRef](#)]
41. Lins Barros, P.; Ein-Mozaffari, F.; Lohi, A. Gas Dispersion in Non-Newtonian Fluids with Mechanically Agitated Systems: A Review. *Processes* **2022**, *10*, 275. [[CrossRef](#)]
42. Jamshidzadeh, M.; Ein-Mozaffari, F.; Lohi, A. Local distribution of oxygen mass transfer coefficient in CMC solutions in bioreactors furnished with different types of coaxial mixers. *Chem. Eng. Res. Des.* **2021**, *174*, 213–224. [[CrossRef](#)]

Disclaimer/Publisher’s Note: The statements, opinions and data contained in all publications are solely those of the individual author(s) and contributor(s) and not of MDPI and/or the editor(s). MDPI and/or the editor(s) disclaim responsibility for any injury to people or property resulting from any ideas, methods, instructions or products referred to in the content.